PHOTONICS Research

Real-time observation of vortex mode switching in a narrow-linewidth mode-locked fiber laser

Jiafeng Lu,[1] Fan Shi,[1] Linghao Meng,[1] Longkun Zhang,[1] Linping Teng,[1] Zhengqian Luo,[2] Peiguang Yan,[3] Fufei Pang,[1,4] and Xianglong Zeng[1,*]

[1]Key Laboratory of Specialty Fiber Optics and Optical Access Networks, Joint International Research Laboratory of Specialty Fiber Optics and Advanced Communication, Shanghai University, Shanghai 200444, China
[2]Department of Electronic Engineering, School of Information Science and Engineering, Xiamen University, Xiamen 361005, China
[3]Shenzhen Key Laboratory of Laser Engineering, Shenzhen University, Shenzhen 518060, China
[4]e-mail: ffpang@shu.edu.cn
*Corresponding author: zenglong@shu.edu.cn

Received 6 January 2020; revised 28 April 2020; accepted 25 May 2020; posted 26 May 2020 (Doc. ID 386954); published 1 July 2020

Temporal and spatial resonant modes are always possessed in physical systems with energy oscillation. In ultrafast fiber lasers, enormous progress has been made toward controlling the interactions of many longitudinal modes, which results in temporally mode-locked pulses. Recently, optical vortex beams have been extensively investigated due to their quantized orbital angular momentum, spatially donut-like intensity, and spiral phase front. In this paper, we have demonstrated the first to our knowledge observation of optical vortex mode switching and their corresponding pulse evolution dynamics in a narrow-linewidth mode-locked fiber laser. The spatial mode switching is achieved by incorporating a dual-resonant acousto-optic mode converter in the vortex mode-locked fiber laser. The vortex mode-switching dynamics have four stages, including quiet-down, relaxation oscillation, quasi mode-locking, and energy recovery prior to the stable mode-locking of another vortex mode. The evolution dynamics of the wavelength shifting during the switching process are observed via the time-stretch dispersion Fourier transform method. The spatial mode competition through optical nonlinearity induces energy fluctuation on the time scale of ultrashort pulses, which plays an essential role in the mode-switching dynamic process. The results have great implications in the study of spatial mode-locking mechanisms and ultrashort laser applications.

https://doi.org/10.1364/PRJ.386954

1. INTRODUCTION

Transient phenomenon dynamics are of significance for revealing the evolution mechanism of numerous nonlinear systems [1–4]. Mode-locked lasers can exhibit profound nonlinear optical dynamics and have moved into the spotlight of optical research due to their unique, intriguing properties of temporal and spatial oscillations [5–9]. Recent years have seen increased interests in mode-locked fiber lasers, largely in anticipation of particle manipulation [10,11], ultrafast laser fabrication [12], high-capacity optical communication [13], and Bose–Einstein condensates [14].

The mode-locked fiber laser provides an ideal platform for exploring ultrashort nonlinear dynamics, where mode-locking (ML) pulses arise from the balance among optical nonlinearity, dispersion, and intracavity gain and loss [15]. Before the ultimate stable ML state, mode-locked lasers experience a series of unstable phenomena when detuned from a steady state or evolve into stable ML pulses from the noise [16]. These instabilities are important, as they reveal the landscape of the pulse evolution during the self-starting process and ML process. The self-starting dynamics in the passively mode-locked fiber lasers have been established by a rich variety of theoretical and experimental results [17–20]. Recently, researchers have pioneered the time-stretch dispersive Fourier transform (TS-DFT) technique for the exploration of build-up dynamics in ML fiber lasers [21–24]. They have revealed detailed information about underlying dynamics in the self-starting process and have generalized the build-up process into three stages: relaxation oscillation, quasi-mode-locking (Q-ML), and stable ML. Polarization change in the laser cavity, energy fluctuation of pump power, and extra environmental perturbations can influence the formation dynamics of the ML pulses. Therefore, the entire observation of the ML process has great implications in the laser operation.

Temporal mode-locked fiber lasers have major influence on both laser physics and practical applications through lasing spatially at the fundamental mode. However, the so-called "capacity crunch" is anticipated, whereby the single-mode fibers

(SMFs) are unable to meet the increasing demand of data telecommunications. At present, the optical spatial division multiplexing (SDM) technique has emerged to provide a promising solution to this potential bandwidth crisis [25,26]. The few-mode fibers (FMFs) and multimode fibers (MMFs) exploited in SDM systems can support a few spatial eigenmodes, each with different propagating constants and spatial distributions. Vortex light multiplexing has obtained great attentions due to its new multiplexing dimension of orbital angular momentum (OAM). Recently, terabit free-space communication employing vortex light has been demonstrated [13]. These modes can interact with each other in the FMFs and MMFs through optical nonlinearity, disorder (random linear mode coupling), and laser gain [27]. The spatial modes' interaction in ultrafast mode-locked fiber lasers is much more interesting and finally evolves into the spatiotemporal ML. Previous reports mainly focus on the overall effect and joint interaction between 10 and 100 spatial modes in spatiotemporal ML, but the specific interaction between the identified individual spatial modes remains to be further explored [28–31].

In this paper, we have demonstrated the first to our knowledge observation of vortex mode-switching dynamics. This result helps scientists understand the rich variety of instability phenomena in the mode-switching dynamic process and the influence of spatial mode interactions on ML states. Previously, static spatial mode switching has been demonstrated in both fiber [32] and free space [33]. Nevertheless, the static mode switching of different spatial modes requires manual adjustment of a polarization controller (PC) or cavity mirror. However, these static mode-switching methods often suffer from the following restrictions: (1) complexity of manual adjustments; (2) low switching speed for capturing the dynamic mode-switching process; and (3) environmental sensitivity. To realize the real-time observation of mode-switching dynamics, here a dual-resonant acousto-optic mode converter (AOMC) is employed to provide a tunable mode switching with fast switching speed in a narrow-linewidth mode-locked laser cavity.

2. THEORY: ACOUSTIC DISPLACEMENT-BASED MODEL OF DUAL-RESONANT AOMC

The AOMC components exploit the electro-acoustic conversion effect in piezoceramic (PZT) materials and the acousto-optic interaction effect in silica fiber media to construct a dynamic tunable spatial mode conversion [34–37]. In our previous reports [38,39], we preliminarily utilized the AOMC in a continuous-wave fiber laser, yet complete theoretical analysis was not demonstrated to reveal the entire property of dual-resonant AOMC. Here we introduce the mode-switching mechanism of AOMC into a mode-locked fiber laser to discover the mode-switching dynamics on ML states, which broadens the practical value of dual-resonant AOMC and enriches the ultrafast physical fundamentals.

The interaction of light beams and acoustic waves enables optical field control in silica fibers, which is mainly derived from the photon–phonon scattering. It is a common belief that a travelling flexural acoustic wave (FAW) produces a periodic micro-bending, which causes an interlaced density of fiber medium as shown in Fig. 1(a). The FAW propagating along the unjacketed silica fiber at the lowest-order mode (F_{11} mode) leads to an acoustically induced displacement vector (AIDV) of $\tilde{u}$ on the fiber medium, which is asymmetric with respect to the direction of applied vibration. Figures 1(b) and 1(c) show a schematic drawing of the AOMC component and a schematic diagram of the fiber end face with an acoustic wave, respectively. Therefore, the permittivity deformation of the

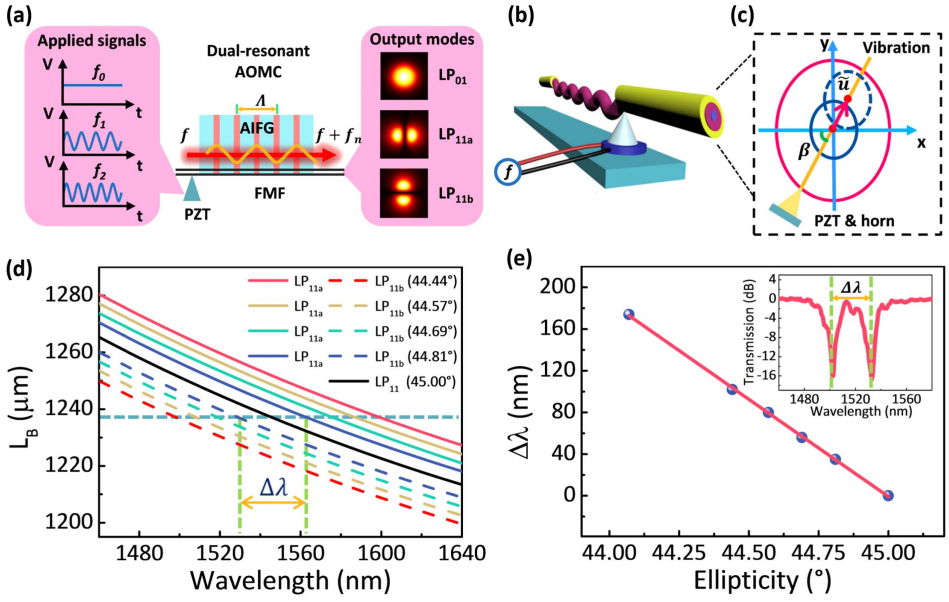

Fig. 1. Diagram of an AOMC and the simulation of the switching mechanism based on optical and acoustic birefringence. (a) The schematic diagram of the dual-resonant AOMC and the mode-switching mechanism. (b) The setup of an AOMC component. (c) The schematic diagram of the fiber end face. (d) The simulation of beat lengths between the LP_{01} mode and $LP_{11a/b}$ modes with different ellipticities of the fiber core. The straight lines and dash lines represent the beat lengths from the LP_{01} mode to the LP_{11a} and LP_{11b} modes, respectively. (e) The $\Delta\lambda$ shifts with the decrease of ellipticity of fiber core. The inset figure shows the wavelength separation in the transmission spectrum of a dual-resonant AOMC.

FAW-endowed ellipse fiber can be classified into two principle contributions [40]: geometric perturbation of ε_g and photoelastic effect of ε_p. The whole effect induced by the FAW on the fiber can be explained via a permittivity deformation as $\delta\hat{\varepsilon}(x,y,z,t) = \delta\varepsilon_g(x,y,z,t) + \delta\varepsilon_p(z,t)$.

A geometrical deformation wave introduces the acoustic displacement and modifies the unperturbed permittivity $\varepsilon_0(x,y)$ as follows:

$$\varepsilon_0(x,y) \to \varepsilon_0(x - u_x, y - u_y), \tag{1}$$

where u_x and u_y represent the orthogonal components of acoustic displacement $\tilde{u}$. The ellipticity of silica fiber leads to an acoustic birefringence, which can be allowed for by making use of the following trigonometric decomposition:

$$\begin{aligned} u_x &= u_0 \cos(Kz - f_n t) \cdot \cos\beta \cdot e^{i\frac{2\pi}{\Lambda_s}}, \\ u_y &= u_0 \cos(Kz - f_n t) \cdot \sin\beta \cdot e^{i\frac{2\pi}{\Lambda_l}}. \end{aligned} \tag{2}$$

Here u_0 represents the amplitude of the acoustic vibration displacement; f_n is the applied frequency of the radio frequency (RF) signal (subscript n refers to different resonant mode conversions). K is the wave vector of the FAW. Axes x and y represent the short and long axes of the fiber in the view of fiber end face, respectively. Axis z is the fiber axial direction. Λ stands for the period of acoustically induced fiber grating (AIFG), which can be expressed as $\Lambda = (\pi \cdot C_{\text{ext}} \cdot R/f_n)^{\frac{1}{2}}$, where $C_{\text{ext}} = 5760$ m/s is the velocity of acoustic wave propagating in silica media. R is the radius of the fiber cladding. In an ellipse fiber, the AIFG periods are different in the two orthogonal directions because the radii of fiber cladding short axis and long axis are different. Therefore, Λ_s and Λ_l are defined as the AIFG periods at the short axis and the long axis, respectively. Angle β is defined as the angle between axis x and the direction of acoustic vibration.

Thus, the geometrically induced correction of permittivity $\delta\varepsilon_g$ can be obtained by utilizing the standard framework of the micro-bending-based model, while the photoelastic correction of permittivity $\delta\varepsilon_p$ can be obtained by combining the photoelastic tensor in the fiber medium, respectively [34,35,40]:

$$\begin{aligned} \delta\varepsilon_g &= \begin{bmatrix} \delta\varepsilon_g^x \\ \delta\varepsilon_g^y \end{bmatrix} = \begin{bmatrix} n_{\text{co}} K^2 u_x \cdot x \\ n_{\text{co}} K^2 u_y \cdot y \end{bmatrix}, \\ \delta\varepsilon_p &= \varepsilon_{\text{co}}^2 p K u_0 \begin{pmatrix} 0 & 0 & 1 \\ 0 & 0 & 0 \\ 1 & 0 & 0 \end{pmatrix} \sin(Kz - f_n t). \end{aligned} \tag{3}$$

Here n_{co} is the refractive index of the fiber core. $\varepsilon_{\text{co}} = n_{\text{co}}^2$ is the permittivity of the fiber core material, and p is the constant of photoelasticity of the fiber medium. The geometric-induced correction has two orthogonal components and further influences the dual-resonant mode conversion in the AOMC.

The mismatching coefficient can be expressed as $\xi = K - \tilde{K}$, where $\tilde{K} = \beta_{01} - \beta_{11}$ is the resonant value of the acoustic wave vector. The propagation constants β_{11a} and β_{11b} are slightly different due to the degeneration of the LP_{11} mode by the ellipticity of the fiber. Therefore, it requires different frequencies of applied RF signals to obtain the mode conversions from the LP_{01} mode to the $LP_{11a/b}$ modes according to the distinct values of the resonant acoustic wave vector. Thus, the mode conversion efficiency can be expressed as [35]

$$K_{a/b} \propto \frac{\pi}{\lambda}\sqrt{\frac{\varepsilon_0}{\mu_0}} n_{\text{co}} \int E_{01}^*(x,y) \cdot \delta\hat{\varepsilon} \cdot E_{11a/b}(x,y)\mathrm{d}x\mathrm{d}y. \tag{4}$$

$K_{a/b}$ represents the conversion efficiencies of mode conversion from the LP_{01} mode to the LP_{11a} and LP_{11b} modes, respectively. $E_{01}(x,y)$ and $E_{11a/b}(x,y)$ are the electric field distributions of the LP_{01} mode and $LP_{11a/b}$ modes, respectively. The overall influence of energy coupling between the LP_{01} mode and the LP_{11} modes exhibits the co-effect of acoustic and optical birefringence. The mode conversions from the LP_{01} mode to the LP_{11a} and LP_{11b} modes have distinct resonances due to the contribution of geometric permittivity deformation. Obviously, the mode conversion can be simply controlled by the AIFG period via tuning the applied RF signals.

Figure 1(d) shows the simulation result of the beat lengths between the LP_{01} mode and the $LP_{11a/b}$ modes with different ellipticities of the adopted FMF. The numerical simulation of the ellipse-fiber-based AIFG employs a finite element method (COMSOL Multiphysics). The step-index FMF adopted in the experiment has a small ellipticity. The ellipticity is defined as $E = \arctan\frac{x}{y}$. Once the frequency of the applied RF signal is set, the period of the AIFG is determined. Here we employ the beat length between different modes to obtain the simulation results. Based on mode coupling theory, the phase-match condition $L_B = \Lambda$ should be satisfied, where $L_B = \lambda \cdot (n_{01} - n_{11a/11b})^{-1}$ is the beat length. Here λ is the resonant wavelength and n_{01} ($n_{11a/11b}$) represents the effective refractive index of the LP_{01} ($LP_{11a/11b}$) mode.

The LP_{11a} and LP_{11b} modes have their own resonant wavelengths, and consequently there exists a wavelength separation ($\Delta\lambda$). As shown in Fig. 1(e), $\Delta\lambda$ has a nearly linear relationship with the ellipticity. The larger the ellipticity, the larger the dual-resonant wavelength separation, which can be used to shape the different optical filters and excite hybrid high-order modes' output with different wavelength combinations.

3. EXPERIMENTAL SETUP AND METHODS

A. AOMC Component Fabrication

Here a thickness-mode PZT is utilized for generating acoustic waves, and the RF signal produced by a function generator is amplified by a high-frequency voltage amplifier (Aigtek: ATA-2022H) as shown in Fig. 1(b). A silica horn adhered to the PZT via epoxy gum is employed for amplifying the acoustic waves and making the acoustic waves from longitudinal mode to transverse mode. A 25 cm long unjacketed fiber is glued to the top of the silica horn. The acoustic wave then propagates along the unjacketed fiber as a flexural mode. The existence of the AIFG structure is determined by the applied RF signal, which means that the AIFG has a dynamic tunability. The transmission spectra are measured via a broadband optical source and an optical spectrum analyzer (OSA, AQ6370, Yokogawa).

In Fig. 2(a), the dual-resonant response is observed, and the mode conversions from the LP_{01} mode to the LP_{11a} and LP_{11b} modes are demonstrated. The resonant depths of the LP_{11a} and LP_{11b} modes are both larger than −15 dB, which means that

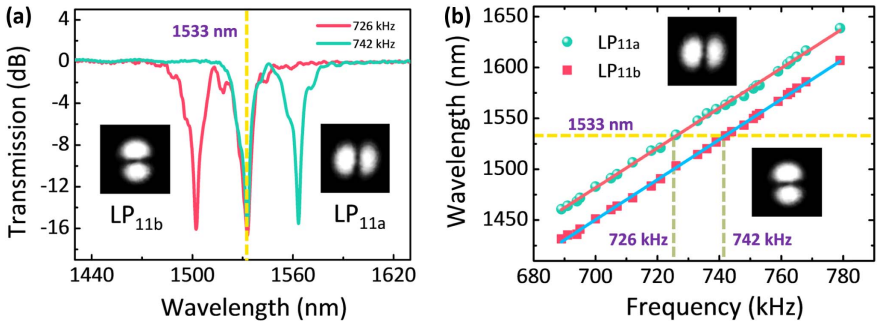

Fig. 2. (a) Transmission spectra of the AOMC with two different applied signal frequencies of 726 kHz and 742 kHz. (b) The frequency shift performance of the applied dual-resonant AOMC.

the mode conversion efficiencies of both the LP_{11a} and LP_{11b} modes are higher than 97%. The ellipticity of the FMF used in the experiment is about 44.81°, and $\Delta\lambda$ is measured to be 30 nm, which agrees well with the theoretical calculation. On the other hand, the mode conversion of LP_{01}–LP_{11a} and LP_{01}–LP_{11b} can be achieved at the same resonant wavelength (1533 nm) by utilizing two different RF frequencies (726 and 742 kHz).

Figure 2(b) shows the center wavelength tuning property of the AOMC dependent on RF frequency. The center wavelengths of the two resonant peaks (LP_{01}–LP_{11a} and LP_{01}–LP_{11b}) both have an approximate linear property of red-shift with the increase of applied RF frequencies. The insets are the corresponding mode patterns of the LP_{11a} and LP_{11b} modes.

B. Experimental Setup of Mode-Locked Fiber Laser

A mode-locked narrow-linewidth fiber laser based on an intracavity AOMC is demonstrated to achieve vortex mode-switching pulses. Narrow-linewidth fiber lasers have the advantages of good stability, high coherence, and low noise [41,42]. The narrow-linewidth mode-locked fiber laser is a good platform for studying spatial mode-switching processes because different spatial mode pulses with narrow linewidth have strong spectral discrimination.

Figure 3(a) shows the schematic of the mode-locked fiber laser setup. The laser oscillator is obtained by using a linear cavity configuration with half cavity of the SMF and half cavity of the FMF. The single-mode cavity consists of a single-mode semiconductor saturable absorption mirror (SESAM), a 50 cm long erbium-doped fiber (EDF), a wavelength-division-multiplexed (WDM) coupler, a 5:95 coupler, and a 10 m long SMF. The few-mode part of the laser cavity consists of a mode stripper (MS), an AOMC, and a few-mode fiber Bragg grating (FM-FBG). The 980 nm laser diode (LD) provides energy pump via a 980–1550 nm wavelength-division multiplexer. The coupler with a 5% output port is employed to extract the laser energy out of the cavity. A 10 m long SMF is inserted into the cavity to optimize the net dispersion. The SESAM-based mode locker is used for forming temporal pulses and reflecting the light back to the laser cavity, simultaneously. The PC_1 is utilized to optimize the ML status by adjusting the birefringence of the linear cavity.

In the FMF part, the MS is exploited to ensure a pure LP_{01} mode light beam propagating into the AOMC because direct splicing between the SMF and the FMF may introduce high-order modes in FMFs. Here the intracavity AOMC achieves a switchable mode conversion from the LP_{01} mode to the $LP_{11a/b}$ modes, while the FM-FBG plays the role of selecting the laser wavelength and reflecting the light back to the cavity. When the high-order mode is reflected and propagates through the AOMC, it will be reconverted to the LP_{01} mode and come back to the SMF cavity. Any unconverted LP_{01} mode is reflected by the FM-FBG and passes through the AOMC, which would convert into the high-order mode and dissipate in the SMF. Therefore, the high purity of the high-order mode is ensured in the few-mode cavity. The PC_2 is utilized to adjust the mode phase and generate OAM modes. The lasing mode at the operation wavelength around 1533 nm is controlled by the applied RF signal frequency (f_n). When the applied RF signal is set to f_1 (726 kHz) or f_2 (742 kHz), the laser operates at the state of the LP_{11a} or LP_{11b} mode, respectively. When the applied RF signal is set to f_0 (a nonresonant frequency or an off state), the laser operates at the state of the LP_{01} mode. To obtain a spatial mode switching in a mode-locked fiber laser, the applied RF signal is modulated via a frequency shift keying (FSK) code, which provides a periodic frequency modulation method for controlling the mode-switching process.

C. Generation of Switching Vortex Pulses

To achieve the generation of vortex pulses, the optical field tuning technique is adopted as follows. First, the LP_{11a} mode and LP_{11b} mode pulses can be rotated with a degree of 45° by PC_2, and the rotated LP_{11} modes can be orthogonally decomposed as $LP_{11a(rot)} = LP_{11}^{even} - LP_{11}^{odd}$ and $LP_{11b(rot)} = LP_{11}^{even} + LP_{11}^{odd}$, respectively.

Actually, the linear polarization modes are only approximations of the eigenmode combinations, including the radially polarized mode (TM_{01}), the azimuthally polarized mode (TE_{01}), and two strictly degenerated hybrid modes ($HE_{21}^{odd}/HE_{21}^{even}$) [43,44]. Therefore, the rotated LP modes can be further expressed by the degeneracies of the eigenmodes:

$$\begin{aligned} LP_{11a(rot)} &= TM_{01} - HE_{21}^{odd} - (TE_{01} + HE_{21}^{even}), \\ LP_{11b(rot)} &= TM_{01} - HE_{21}^{odd} + (TE_{01} + HE_{21}^{even}). \end{aligned} \quad (5)$$

Then the stress provided by PC_2 changes the effective dimensions of the FMF, resulting in different phase velocities of the

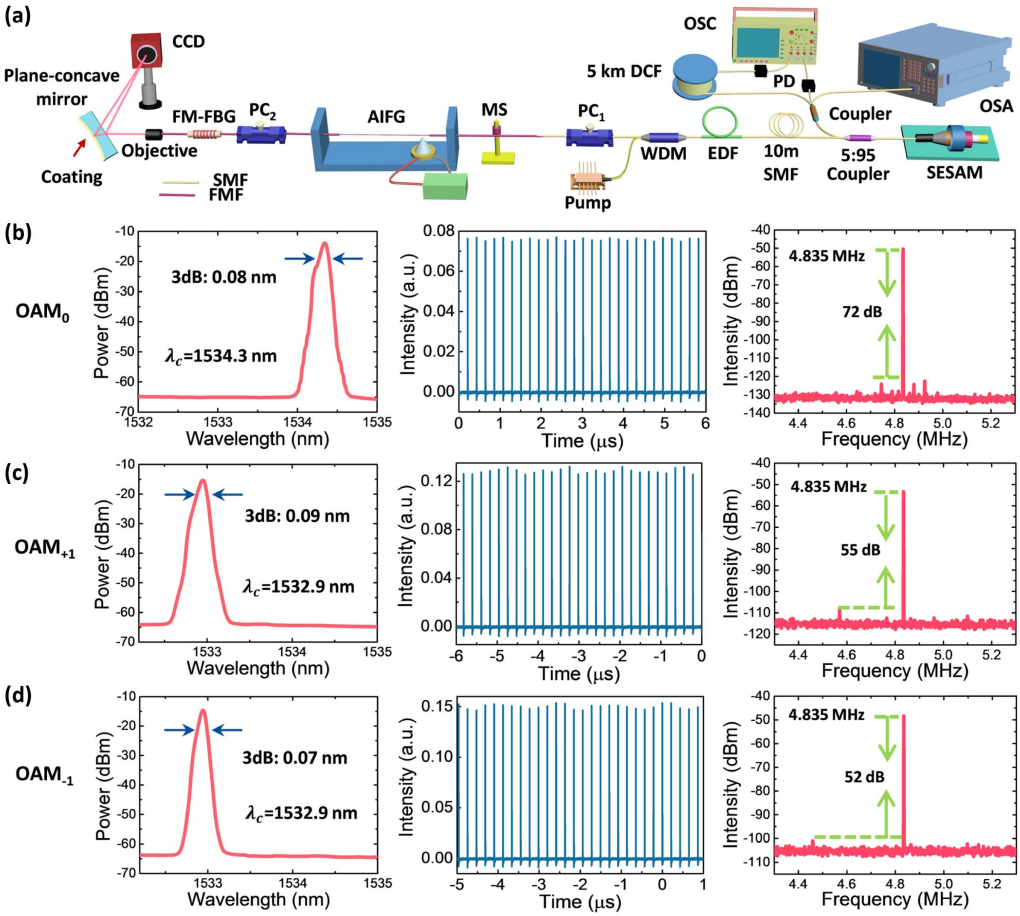

Fig. 3. Experimental setup and results of spatial mode switching in a mode-locked fiber laser. (a) The schematic diagram of the spatial mode switching fiber laser setup. OSA, optical spectrum analyzer; WDM, wavelength-division multiplexer; PC, polarization controller; MS, mode stripper. The stable ML with three different mode states: (b) OAM_0, (c) OAM_{+1}, and (d) OAM_{-1}. The results include laser spectra, pulse trains, and RF signals (see spatial mode-switching processes of LP_{01}–LP_{11a}, LP_{01}–LP_{11b}, LP_{11a}–LP_{11b}, and OAM_{+1}–OAM_{-1} in Visualization 1, Visualization 2, Visualization 3, and Visualization 4, respectively).

eigenmodes. When tuning the stress appropriately, a phase difference of "$\pi/2$" ("i") can be changed to the eigenmodes. Finally, the adjusted LP_{11a} mode and LP_{11b} mode become the corresponding −1st-order OAM mode and +1st-order OAM mode and can be expressed as

$$\begin{aligned} LP_{11a(adj)} &= TM_{01} - HE_{21}^{odd} - iTE_{01} - iHE_{21}^{even} = OAM_{-1}, \\ LP_{11b(adj)} &= TM_{01} - HE_{21}^{odd} + iTE_{01} + iHE_{21}^{even} = OAM_{+1}. \end{aligned} \tag{6}$$

Thus, the mode-switching OAM pulses are successfully demonstrated by altering the applied RF signal frequency.

4. RESULTS

A. Mode-Locked Fiber Laser with OAM Mode-Switching Output

The OAM-switching pulses with the topology numbers of +1 and −1 are successfully demonstrated. Figures 3(b)–3(d) exhibit the outputs of the mode-locked fiber laser at three different vortex modes: OAM_0 (LP_{01} mode), OAM_{+1}, and OAM_{-1}, respectively. The laser spectra show a wavelength difference due to the different reflection wavelengths of the FM-FBG with the OAM_0 mode and OAM_1 mode. The laser operating wavelengths of the OAM_0 mode and OAM_1 mode are 1534.3 nm and 1532.9 nm, respectively. Due to the narrow bandwidth of the FM-FBG reflection, the 3 dB widths of the laser spectra at the ML states of OAM_0, OAM_{+1}, and OAM_{-1} are 0.09, 0.07, and 0.08 nm, respectively. The pulse trains recorded by a real-time oscilloscope (OSC, Keysight, DSOS404A) via a high-speed photoelectric detector (PD) confirm the stable mode-locked states of the three OAM modes.

The repetition rate of the mode-locked fiber laser is 4.835 MHz, which agrees well with the calculated one corresponding to the cavity length (~21.5 m, and the repetition rate is 4.81 MHz). The operating vortex mode states are modulated by modulating the applied RF signal frequency rather than changing the laser cavity so that the repetition rate has no difference in the three vortex modes. However, the signal-to-noise ratio (SNR) has lower values at the states of the OAM_1 modes than of the OAM_0 mode, since mode conversion introduces intracavity modal perturbation and slightly declines the SNR.

The interference patterns are obtained by employing a plane-concave mirror (PCM)-based interference technique [45,46]. The OAM-switching pulsed laser beam is collimated by using an objective lens and is then reflected by the PCM as shown in Fig. 3(a). The concave face of the mirror is coated with a reflectivity of >99% at 1550 nm, while the plane face of the mirror is uncoated. Therefore, when the OAM pulsed laser beam is incident into the PCM, both the plane face (Fresnel reflection ~4% at 1550 nm) and the concave face (>99% at 1550 nm) reflect the laser beam. The two reflected laser beams are overlapped and spatially interfered at the cross point by properly adjusting the position and the angle of the PCM.

The mode patterns as well as interference patterns are recorded by using the charge-coupled device (CCD, InGaAs camera, model C10633-23, from Hamamatsu Photonics) as depicted in Fig. 4(a). As seen in Fig. 4(b), the pulse widths of the three modes are measured to be approximately 400 ps.

The slope efficiencies of three distinct mode states are demonstrated as shown in Fig. 4(c). The slope efficiencies of the OAM_0, OAM_{+1}, and OAM_{-1} modes are 5.5%, 7.13%, and 7.64%, respectively. The distinction between the slope efficiencies of two OAM_1 modes is because of the slight difference of mode conversion efficiency. Additionally, the difference between the slope efficiencies of the OAM_0 mode and the OAM_1 mode is mainly due to the reflectivity difference of the FM-FBG.

B. Real-Time Observation of Vortex Mode Switching in the Mode-Locked Fiber Laser

Vortex mode switching introduces intracavity perturbation, and the mode-switching dynamics become an interesting phenomenon. Real-time pulse evolution in the mode-switching process is demonstrated as depicted in Fig. 5. OAM mode switching causes a quasi-broken and reconstruction process of the ML states. The pulse train signals in Fig. 5(a) reveal that there exists an evident laser strike region before the appearance of a stable pulse train (i.e., the stable ML state) in every OAM mode-switching process.

Figures 5(b) and 5(c) exhibit the corresponding detailed information of every laser strike region of the mode-switching process named as **I–VI**. Additionally, strike region **I** (mode switching from the OAM_0 mode to the OAM_{-1} mode) and **II** (mode switching from the OAM_{-1} mode to the OAM_{+1} mode) are interpreted particularly. The duration times of the whole strike region are ~1 ms (between the OAM_0 mode and OAM_{-1} mode), ~1.8 ms (between the OAM_{-1} mode and OAM_{+1} mode), and ~2.2 ms (between the OAM_0 mode and OAM_{+1} mode).

As shown in Fig. 5, the experimental results reveal that the whole mode-switching dynamic process includes a quiet-down state, relaxation oscillation, Q-ML stage, and finally the reconstructed ML phase. At the beginning of the strike region, there exists a quiet-down process, which is mainly on account of the microstructure change of the AIFG, such as the fiber long-period grating formation (OAM_0–OAM_1), grating collapse (OAM_1–OAM_0), and period variation (OAM_{-1}–OAM_{+1}).

The time durations of the three kinds of quiet-down processes are ~120, ~50, and ~80 μs, respectively, which correspond to the switching times of the AOMC. Note that all the quiet-down times are marginally smaller than the switching time of the AOMC component measured in Ref. [38], because a partial mode perturbation is enough for destroying

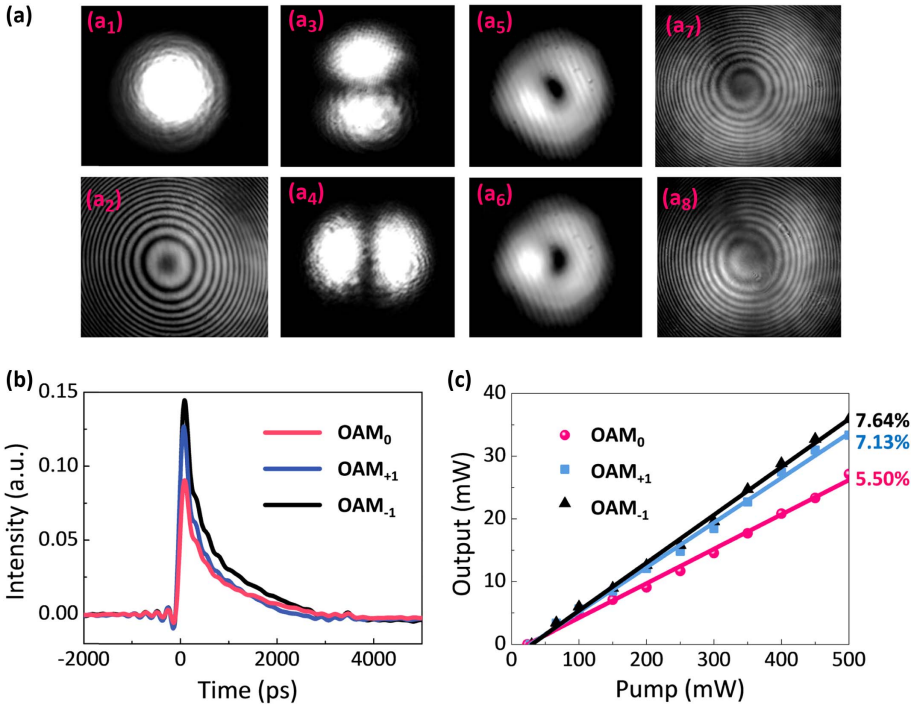

Fig. 4. Output results of the mode-switching mode-locked fiber laser. (a) The mode patterns recorded by a CCD include the (a_1) mode intensity pattern and (a_2) interference pattern of the OAM_0 mode; (a_3), (a_4) LP_{11} mode intensity patterns, (a_5), (a_6) donut mode patterns; and (a_7), (a_8) interference patterns of the OAM_{+1} and OAM_{-1} modes. (b) The real-time pulse shapes of three OAM modes. (c) The slope efficiencies of the mode-locked fiber laser with three OAM mode states.

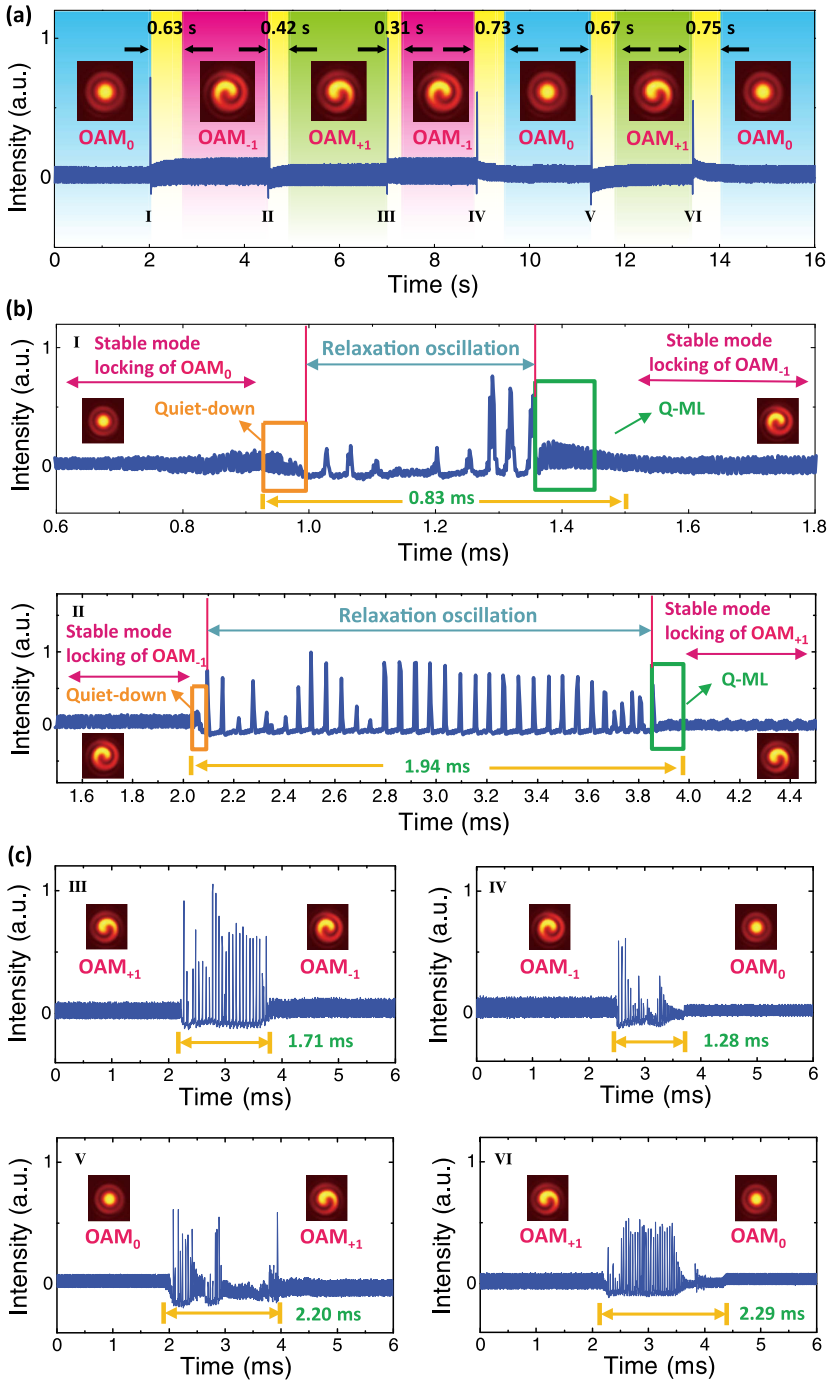

Fig. 5. Real-time information of mode-switching dynamics. (a) The real-time information of the whole mode-switching dynamic process among three vortex modes (OAM_0, OAM_{-1}, and OAM_{+1}). The detailed information of the strike regions named as (b) **I**, **II** and (c) **III**–**VI**.

the stable ML state and introducing the instability in the laser cavity. Then the number of cavity photons comes to an initial low value as determined by quantum field fluctuation.

After a short time, a series of laser strikes is generated, which is mainly originated from the relaxation oscillation. The separation of the neighboring laser strikes is ~70 μs. Liu *et al.* reported a raised relaxation oscillation phenomenon in the build-up process in mode-locked fiber lasers [21]. Differently, the laser strikes observed in this experiment are not the regularly raising type, which is mainly modulated by the spatial mode competition. Spatially lasing modes can interact through the optical nonlinearity at the time scale of a mode-locked pulse, which leads to an energy fluctuation in the temporal and spatial domains. Additionally, the rare-earth gain media introduce a temporally averaging nonlinear interaction in the relaxation oscillation process [28, 47]. Prior to the stable ML state formation, there co-exist two modes (i.e., the original mode and the target converted mode) and their intermediate states.

The competition of these spatial modes leads to a fluctuation of energy accumulation in the cavity and further influences the amplitude of the formed laser strikes. It is worth noting that the mode competition between two OAM_1 modes is weaker than that between the OAM_0 mode and the OAM_1 mode. Hence, the peak envelope change of laser strikes during the process of mode switching between two OAM_1 modes is much weaker than that between the OAM_0 mode and OAM_1 modes. The Q-ML is also observed in the temporal information with a duration time of ~120 μs. Typical pulses arise and form a pulse train with the shifting of laser wavelength (detailed discussion in the next section).

The final reconstructed ML state has two stages including temporal stable ML and temporal-amplitude stable ML. At the beginning of the reconstructing ML state, the pulse train has a recovery time to obtain a stable energy level of pulse amplitude. The recovery time between the OAM_0 mode and the OAM_1 mode is ~0.7 s, while it is ~0.4 s between two OAM_1 modes. The laser oscillating and reconstructing processes between different OAM modes are much more difficult than those between same-order modes, and thus it takes more time for recovering ML pulses.

C. Vortex Mode-Switching Dynamics Observed by TS-DFT Method

To overcome the limited electronic bandwidth of the real-time OSC, the TS-DFT method is exploited to reveal the detailed spectral and temporal information of the transient vortex OAM mode-switching process in the mode-locked laser. As shown in Fig. 3(a), the real-time spectral information is obtained from the dispersing pulses detected after a dispersion compensation fiber (DCF). The dispersion (D) and length (L) of the employed DCF are −648 ps · nm^{-1} · km^{-1} and ~5 km, respectively. The spectral information can be mapped into the temporal waveform recorded by an OSC. The mapping relationship between temporal and spectral resolutions can be expressed as $\Delta t = |D| \cdot L \cdot \Delta\lambda = 3.24\ \text{ns} \cdot \text{nm}^{-1} \cdot \Delta\lambda$, where Δt and $\Delta\lambda$ represent the temporal and spectral resolutions, respectively. Besides, the round-trip time is 206.8 ns.

Figure 6 shows the experimental observation of vortex mode switching from the OAM_{+1} mode to the OAM_0 mode via the TS-DFT method. Since the lasing wavelengths of the OAM_{+1} mode and the OAM_0 mode are different, the spectrum evolution exhibits a corresponding wavelength change of OAM-switching pulses. Figure 6(a) depicts the energy envelope evolution of the vortex OAM mode-switching dynamic process. Note that the end of this data shows a fluctuation after round-trips of ~6000 (corresponding to time of ~1.24 ms). According to Fig. 5(c-VI), the duration time of the whole laser strike process is 2.29 ms, which means there exists an energy fluctuation process in the tail part of the laser strike region.

Figure 6(b) shows the whole spectrum evolution dynamics. First, the laser cavity operates at the stable OAM_{+1} mode. As depicted in Fig. 6(b_1), the single-shot spectrum shows a stable state at the wavelength of ~1532.9 nm. When the applied RF signal changes, the stable ML state collapses, and the laser output evolves as a quantum initial situation, which is characterized as a low-energy state. As enough cavity energy accumulates, there arise some laser spikes that mainly originate from the variation of population inversion in the EDF as shown in Fig. 6(b_2). The laser spikes vary irregularly until one laser spike dominates the energy fluctuation. Then the laser operating wavelength goes through a shift process to the final targeted lasing wavelength (1534.3 nm) of the OAM_0 mode as shown in Fig. 6(b_3). Figures 6(c_1) and 6(c_2) show the DFT signals and optical spectra of stable ML states of the OAM_{+1} mode and OAM_0 mode, respectively, which are well matched with each other.

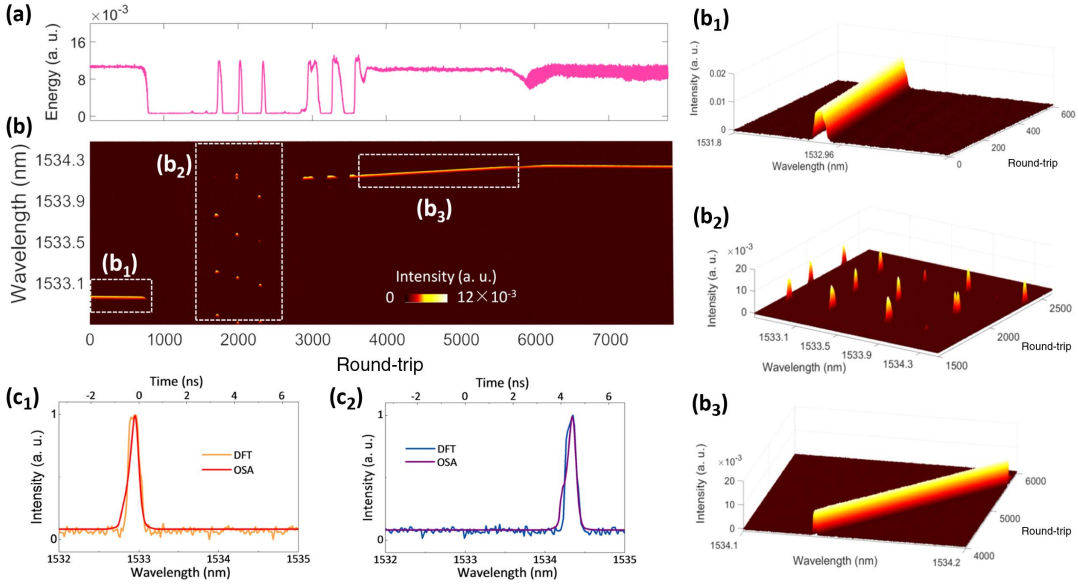

Fig. 6. Experimental observation of vortex mode switching from the OAM_{+1} mode to the OAM_0 mode via the TS-DFT method. (a) The energy envelope evolution of the DFT signal. (b) The whole spectrum evolution of the vortex mode-switching dynamics with closeup pictures of (b_1) initial ML, (b_2) laser spikes, and (b_3) wavelength shift. Comparisons of DFT signals and optical spectra of the (c_1) OAM_{+1} mode and (c_2) OAM_0 mode (see the dynamic single-shot spectrum evolution in Visualization 5).

5. CONCLUSION

In this work, we have experimentally demonstrated the vortex mode-switching dynamics in a mode-locked fiber laser by introducing the mode-switchable AOMC. The real-time pulse evolution exhibits that a mode-switching process mainly consists of a quiet-down moment, a relaxation oscillation process, a Q-ML stage, and an energy recovering process. The vortex mode-switching dynamics provides a new way to study the formation process of ML pulses under the view of spatial degree of freedom. In the mode-switching dynamic process, we found that the energy fluctuation of mode switching between different vortex modes is strong enough to form irregular laser strikes. Hence, most likely the mode conversion and mode competition inside the laser cavity are responsible for the energy perturbation. The energy perturbation is supposed to be the main factor affecting the pulse evolution dynamic process. Furthermore, the unveiled evolution process of spatial mode switching is currently instructive for the development of ultrafast lasers and transient nonlinearity. The experimental result of vortex mode-switching dynamics reveals the physical mechanism of a vortex mode state transition process in a mode-locked fiber laser, which enriches the ultrafast photonics and advances the practical applications.

In addition, the novel result of generating switching optical vortex pulses is also demonstrated and paves the way toward quantum information science [48], stimulated emission depletion microscopy (STED) [49], and ultrafast laser fabrication [50]. For instance, traditional vortex mode converters employed in quantum optical communication are free-space elements that need complicated optical alignment to the fiber system. Our method of generating switchable vortex modes has the following advantages: (1) eliminate the space-fiber coupling process due to the all-fiber configuration and (2) allow marshalling of data information by dynamic switching. Our method of generating a switchable vortex beam provides a switchable light source between Gaussian distribution and donut distribution in STED systems. The fluorescent radiation and stimulated depletion can be flexibly controlled by mode switching between the zeroth-order and first-order vortex modes. In field of laser fabrication, the switchable OAM ultrafast laser pulses can enrich the types of nanostructures fabricated by vortex laser and broaden the dimensions of vortex laser processing. For example, chiral-alternating nanogratings can be fabricated by switching the OAM_{+1} mode and OAM_{-1} mode alternatively.

Meanwhile, the detailed AIDV-based model of a dual-resonant AOMC further enriches the physical mechanism of acoustic and optical birefringence and gives an instructive pathway for extending the practical applications of the AOMCs. Consequently, all these findings will enable the development of a new class of strategies for studying the ML mechanism through controlling the spatial mode switching.

Funding. National Key Research and Development Program of China (2018YFB1801800); National Natural Science Foundation of China (91750108, 61635006); 111 Project (D20031).

Acknowledgment. X. Zeng acknowledges the support of the Program for Professor of Special Appointment (Eastern Scholar) at Shanghai Institutions of Higher Learning. We are grateful to Dr. Junsong Peng at East China Normal University for invaluable discussions on ML dynamics.

Disclosures. The authors declare no conflicts of interest.

REFERENCES

1. K. Goda, K. K. Tsia, and B. Jalali, "Serial time-encoded amplified imaging for real-time observation of fast dynamic phenomena," Nature **458**, 1145–1149 (2009).
2. H. Guo, M. Karpov, E. Lucas, A. Kordts, M. H. P. Pfeiffer, G. Lichachev, V. E. Lobanov, M. L. Gorodetsky, and T. J. Kippenberg, "Universal dynamics and deterministic switching of dissipative Kerr solitons in optical microresonators," Nat. Phys. **13**, 94–102 (2017).
3. B. Li, S. W. Huang, Y. Li, C. W. Wong, and K. K. Y. Wong, "Panoramic-reconstruction temporal imaging for seamless measurements of slowly-evolved femtosecond pulse dynamics," Nat. Commun. **8**, 61 (2017).
4. J. Kim and Y. Song, "Ultralow-noise mode-locked fiber lasers and frequency combs: principles, status, and applications," Adv. Opt. Photon. **8**, 465–540 (2016).
5. U. Teğin, E. Kakkava, B. Rahmani, D. Psaltis, and C. Moser, "Spatiotemporal self-similar fiber laser," Optica **6**, 1412–1415 (2019).
6. T. Mayteevarunyoo, B. A. Malomed, and D. V. Skryabin, "Spatiotemporal dissipative solitons and vortices in a multi-transverse-mode fiber laser," Opt. Express **27**, 37364–37373 (2019).
7. U. Teğin, B. Rahmani, E. Kakkava, N. Borhani, C. Moser, and D. Psaltis, "Controlling spatiotemporal nonlinearities in multimode fibers with deep neural networks," APL Photon. **5**, 030804 (2019).
8. S. V. Smirnov, S. Sugavanam, O. A. Gorbunov, and D. V. Churkin, "Generation of spatio-temporal extreme events in noise-like pulses NPE mode-locked fibre laser," Opt. Express **25**, 23122–23127 (2017).
9. H. Wu, C. Huang, and J. Huang, "Spatiotemporal dynamics of a passively mode-locked Nd:$GdVO_4$ laser," Opt. Express **15**, 2391–2397 (2007).
10. M. Padgett and R. Bowman, "Tweezers with a twist," Nat. Photonics **5**, 343–348 (2011).
11. D. G. Grier, "A revolution in optical manipulation," Nature **424**, 810–816 (2003).
12. S. Kawata, H. B. Sun, T. Tanaka, and K. Takada, "Finer features for functional microdevices," Nature **412**, 697–698 (2001).
13. J. Wang, J. Y. Yang, I. M. Fazal, N. Ahmed, Y. Yan, H. Huang, Y. Ren, Y. Yue, S. Dolinar, M. Tur, and A. E. Willner, "Terabit free-space data transmission employing orbital angular momentum multiplexing," Nat. Photonics **6**, 488–496 (2012).
14. J. Denschlag, J. Simsarian, D. Feder, C. W. Clark, L. Collins, J. Cubizolles, L. Deng, E. W. Hagley, K. Helmerson, and W. P. Reinhardt, "Generating solitons by phase engineering of a Bose-Einstein condensate," Science **287**, 97–101 (2000).
15. A. F. J. Runge, N. G. R. Broderick, and M. Erkintalo, "Observation of soliton explosions in a passively mode-locked fiber laser," Optica **2**, 36–39 (2015).
16. P. Ryczkowski, M. Närhi, C. Billet, J.-M. Merolla, G. Genty, and J. M. Dudley, "Real-time full-field characterization of transient dissipative soliton dynamics in a mode-locked laser," Nat. Photonics **12**, 221–227 (2018).
17. F. Krausz, T. Brabec, and C. Spielmann, "Self-starting passive mode locking," Opt. Lett. **16**, 235–237 (1991).
18. E. Kelleher and J. Travers, "Chirped pulse formation dynamics in ultra-long mode-locked fiber lasers," Opt. Lett. **39**, 1398–1401 (2014).
19. A. Chong, L. Wright, and F. Wise, "Ultrafast fiber lasers based on self-similar pulse evolution: a review of current progress," Rep. Prog. Phys. **78**, 113901 (2015).
20. J. Peng and H. Zeng, "Build-Up of dissipative optical soliton molecules via diverse soliton interactions," Laser Photon. Rev. **12**, 1800009 (2018).
21. X. Liu and Y. Cui, "Revealing the behavior of soliton buildup in a mode-locked laser," Adv. Photon. **1**, 016003 (2019).

22. Y. Cui and X. Liu, "Revelation of the birth and extinction dynamics of solitons in SWNT-mode-locked fiber lasers," Photon. Res. **7**, 423–430 (2019).
23. X. Liu and M. Pang, "Revealing the buildup dynamics of harmonic mode-locking states in ultrafast lasers," Laser Photon. Rev. **13**, 1800333 (2019).
24. X. Liu, D. Popa, and N. Akhmediev, "Revealing the transition dynamics from *Q* switching to mode locking in a soliton laser," Phys. Rev. Lett. **123**, 093901 (2019).
25. D. J. Richardson, J. M. Fini, and L. E. Nelson, "Space-division multiplexing in optical fibres," Nat. Photonics **7**, 354–362 (2013).
26. H. R. Stuart, "Dispersive multiplexing in multimode optical fiber," Science **289**, 281–283 (2000).
27. L. G. Wright, Z. M. Ziegler, P. M. Lushnikov, Z. Zhu, M. A. Eftekhar, D. N. Christodoulides, and F. W. Wise, "Multimode nonlinear fiber optics: massively parallel numerical solver, tutorial, and outlook," IEEE J. Sel. Top. Quantum Electron. **24**, 5100516 (2018).
28. L. G. Wright, D. N. Christodoulides, and F. W. Wise, "Spatiotemporal mode-locking in multimode fiber lasers," Science **358**, 94–97 (2017).
29. W. H. Renninger and F. W. Wise, "Optical solitons in graded-index multimode fibres," Nat. Commun. **4**, 1719 (2013).
30. L. G. Wright, D. N. Christodoulides, and F. W. Wise, "Controllable spatiotemporal nonlinear effects in multimode fibres," Nat. Photonics **9**, 306–310 (2015).
31. H. Qin, X. Xiao, P. Wang, and C. Yang, "Observation of soliton molecules in a spatiotemporal mode-locked multimode fiber laser," Opt. Lett. **43**, 1982–1985 (2018).
32. R. Chen, F. Sun, J. Yao, J. Wang, H. Min, A. Wang, and Q. Zhan, "Mode locked all-fiber laser generating optical vortex pulses with tunable repetition rate," Appl. Phys. Lett. **112**, 261103 (2018).
33. Z. Li, J. Peng, Q. Li, Y. Gao, J. Li, and Q. Cao, "Generation of picosecond vortex beam in a self-mode-locked Nd:YVO_4 laser," Optoelectron. Lett. **13**, 188–191 (2017).
34. S. D. Lim, H. C. Park, I. K. Hwang, and B. Y. Kim, "Combined effects of optical and acoustic birefringence on acousto-optic mode coupling in photonic crystal fiber," Opt. Express **16**, 6125–6133 (2008).
35. W. Zhang, K. Wei, L. Huang, D. Mao, B. Jiang, F. Gao, G. Zhang, T. Mei, and J. Zhao, "Optical vortex generation with wavelength tunability based on an acoustically-induced fiber grating," Opt. Express **24**, 19278–19285 (2016).
36. P. Z. Dashti, F. Alhassen, and H. P. Lee, "Transfer of orbital angular momentum between acoustic and optical vortices in optical fiber," Phys. Rev. Lett. **96**, 043064 (2006).
37. Y. Li, L. Huang, H. Han, L. Gao, Y. Cao, Y. Gong, W. Zhang, F. Gao, I. P. Ikechukwu, and T. Zhu, "Acousto-optic tunable ultrafast laser with vector-mode-coupling-induced polarization conversion," Photon. Res. **7**, 798–805 (2019).
38. J. Lu, L. Meng, F. Shi, X. Liu, Z. Luo, P. Yan, L. Huang, F. Pang, T. Wang, X. Zeng, and P. Zhou, "Dynamic mode-switchable optical vortex beams using acousto-optic mode converter," Opt. Lett. **43**, 5841–5844 (2018).
39. J. Lu, L. Meng, F. Shi, and X. Zeng, "A mode-locked fiber laser with switchable high-order modes using intracavity acousto-optic mode converter," in *Optical Fiber Communication Conference (OFC)* (2019), paper W3C.3.
40. M. A. Yavorsky, D. V. Vikulin, E. V. Barshak, B. P. Lapin, and C. N. Alexeyev, "Revised model of acousto-optic interaction in optical fibers endowed with a flexural wave," Opt. Lett. **44**, 598–601 (2019).
41. R. Li, J. Zou, W. Li, K. Wang, T. Du, H. Wang, X. Sun, Z. Xiao, H. Fu, and Z. Luo, "Ultrawide-space and controllable soliton molecules in a narrow-linewidth mode-locked fiber laser," IEEE Photon. Technol. Lett. **30**, 1423–1426 (2018).
42. Y. Shen, G. Ren, Y. Yang, S. Yao, Y. Wu, Y. Jiang, Y. Xu, W. Jin, and S. Jian, "Switchable narrow linewidth fiber laser with LP_{11} transverse mode output," Opt. Laser Technol. **98**, 1–6 (2018).
43. S. Ramachandran and P. Kristensen, "Optical vortices in fibers," Nanophotonics **2**, 455–474 (2013).
44. J. Wang and A. E. Willner, "Twisted communications using orbital angular momentum (Tutorial Talk)," in *Optical Fiber Communication Conference*, OSA Technical Digest (online) (2016), paper Th1H.5.
45. J. Zou, H. Wang, W. Li, T. Du, B. Xu, N. Chen, Z. Cai, and Z. Luo, "Visible-wavelength all-fiber vortex laser," IEEE Photon. Technol. Lett. **31**, 1487–1490 (2019).
46. J. Zou, Z. Kang, R. Wang, H. Wang, J. Liu, C. Dong, X. Jiang, B. Xu, Z. Cai, G. Qin, H. Zhang, and Z. Luo, "Green/red pulsed vortex-beam oscillations in all-fiber lasers with visible-resonance gold nanorods," Nanoscale **11**, 15991–16000 (2019).
47. Z. Qin, G. Xie, H. Gu, T. Hai, P. Yuan, J. Ma, and L. Qian, "Mode-locked 2.8-μm fluoride fiber laser: from soliton to breathing pulse," Adv. Photon. **1**, 065001 (2019).
48. A. Mair, A. Vaziri, G. Weihs, and A. Zeilinger, "Entanglement of the orbital angular momentum states of photons," Nature **412**, 313–316 (2001).
49. L. Yan, P. Gregg, E. Karimi, A. Rubano, L. Marrucci, R. Boyd, and S. Ramachandran, "*Q*-plate enabled spectrally diverse orbital-angular-momentum conversion for stimulated emission depletion microscopy," Optica **2**, 900–903 (2015).
50. J. Lu, Y. Dai, Q. Li, Y. Zhang, C. Wang, F. Pang, T. Wang, and X. Zeng, "Fiber nanogratings induced by femtosecond pulse laser direct writing for in-line polarizer," Nanoscale **11**, 908–914 (2019).